minerals

MDPI

Article

First Terrestrial Occurrence of Kaitianite ($Ti^{3+}{}_2Ti^{4+}O_5$) from the Upper Mantle beneath Mount Carmel, Israel

Chi Ma [1,*], Fernando Cámara [2], Luca Bindi [3], Vered Toledo [4] and William L. Griffin [5,6,*]

1 Division of Geological and Planetary Sciences, California Institute of Technology, Pasadena, CA 91125, USA
2 Dipartimento di Scienze della Terra "A. Desio", Università degli Studi di Milano, I-20133 Milan, Italy; fernando.camara@unimi.it
3 Dipartimento di Scienze della Terra, Università degli Studi di Firenze, I-50121 Florence, Italy; luca.bindi@unifi.it
4 Shefa Gems (A.T.M.) Ltd., Netanya 4210602, Israel
5 Australian Research Council Centre of Excellence for Core to Crust Fluid Systems (CCFS), Macquarie University, Sydney, NSW 2109, Australia
6 GEMOC ARC National Key Centre, Macquarie University, Sydney, NSW 2109, Australia
* Correspondence: chima@caltech.edu (C.M.); bill.griffin@mq.edu.au (W.L.G.)

Abstract: Our nanomineralogical investigation of melt inclusions in corundum xenoliths from the Mount Carmel area, Israel, has revealed seven IMA-approved new minerals since 2021. We report here the first terrestrial occurrence of kaitianite ($Ti^{3+}{}_2Ti^{4+}O_5$). Kaitianite occurs as exsolution lamellae in tistarite (Ti_2O_3), in a melt inclusions together with a Ti,Al,Zr-oxide, a $MgTi^{3+}{}_2Al_4SiO_{12}$ phase, spinel, sapphirine, Ti-sulfide, alabandite, and Si-rich glass in a corundum grain (Grain 1125C2). The chemical composition of kaitianite using electron probe microanalysis is (wt%) Ti_2O_3 58.04, TiO_2 37.82, Al_2O_3 2.87, MgO 0.85, ZrO_2 0.10, CaO 0.02, SiO_2 0.02, sum 99.73, yielding an empirical formula of $(Ti^{3+}{}_{1.78}Al_{0.12}Ti^{4+}{}_{0.05}Mg_{0.05})(Ti^{4+}{}_{1.00})O_5$, with the Ti^{3+} and Ti^{4+} partitioned, assuming a stoichiometry of three cations and five oxygen anions pfu. Electron back-scatter diffraction reveals that kaitianite has the monoclinic $C2/c$ γ-Ti_3O_5-type structure with cell parameters: a = 10.12 Å, b = 5.07 Å, c = 7.18 Å, β = 112°, V = 342 Å^3, and Z = 4. Kaitianite is a high-temperature oxide phase, formed in melt pockets under reduced conditions in corundum-aggregate xenoliths derived from the upper mantle beneath Mount Carmel, Israel.

Keywords: kaitianite; $Ti^{3+}{}_2Ti^{4+}O_5$; tistarite; high-temperature oxides; melt inclusions; corundum; Mount Carmel; Israel

check for updates

Citation: Ma, C.; Cámara, F.; Bindi, L.; Toledo, V.; Griffin, W.L. First Terrestrial Occurrence of Kaitianite ($Ti^{3+}{}_2Ti^{4+}O_5$) from the Upper Mantle beneath Mount Carmel, Israel. *Minerals* **2023**, *13*, 1097. https://doi.org/10.3390/min13081097

Academic Editor: Joel E. Gagnon

Received: 21 July 2023
Revised: 6 August 2023
Accepted: 14 August 2023
Published: 17 August 2023

1. Introduction

Super-reduced mineral assemblages are found worldwide in association with explosive volcanism (kimberlites, alkali basalts, tholeiitic basalts) and in ophiolites associated with deep subduction at continental plate margins [1–3]. Their origin has been controversial, with claims that they are of anthropogenic origin. The well-documented material found as xenoliths and xenocrysts in small Cretaceous volcanoes and the associated Plio–Pleistocene gem placer deposits at Mount Carmel, northern Israel, are important in this regard because the geological setting, geochemical data, and geochronology effectively rule out any realistic suggestion of human intervention [4–6]. Many of the super-reduced phases are found as inclusions in xenoliths of corundum aggregates, and the relationships of different phases in melt inclusions have been critical to understanding the genesis of the super-reduced magma-fluid systems.

During our ongoing nanomineralogical investigation of melt inclusions in the corundum xenocrysts, we have identified seven IMA-approved new minerals since 2021: griffinite (Al_2TiO_5), magnéliite ($Ti^{3+}{}_2Ti^{4+}{}_2O_7$), ziroite ($ZrO_2$), sassite ($Ti^{3+}{}_2Ti^{4+}O_5$), mizraite-(Ce) ($Ce(Al_{11}Mg)O_{19}$), toledoite (TiFeSi), and yeite (TiSi) [7–13]. Reported here are the first terrestrial, and second natural, occurrences of kaitianite ($Ti^{3+}{}_2Ti^{4+}O_5$) in a corundum xenocryst

from Mount Carmel, providing more insights into the origin of reduced high-temperature minerals from the upper mantle. Kaitianite was first discovered in the Allende CV3 meteorite as a refractory mineral formed in the solar nebula [14].

2. Materials and Methods

The studied corundum xenoliths were found to occur in the pyroclastic ejecta of small Cretaceous basaltic volcanoes exposed on Mount Carmel and in placer gemstone deposits in the terraces of the Paleocene to Pleistocene proto-Kishon River, which now drains Mount Carmel and enters the sea near Haifa in northern Israel [2] as well as the tributary Mizra river. Some of the xenolithic material in the paleoterrace deposits may also have derived from Miocene to Paleocene basalts outcropping in the drainage of the Kishon River. The xenoliths are aggregates of skeletal corundum crystals with melt pockets containing reduced mineral assemblages [1,4,15–17]. The kaitianite material described here is found in corundum Grain 1125C2 in polished Mount Carmel mount Corundum-18-1.

An electron probe microanalyzer (EPMA), a high-resolution scanning electron microscope (SEM) with X-ray energy dispersive spectrometer (EDS), and electron backscatter diffraction (EBSD) were used to characterize the composition and structure of kaitianite and associated phases. A ZEISS 1550VP Field-Emission SEM (ZEISS Group, Oberkochen, Germany) with an Oxford X-Max EDS (Oxford Instruments, Abingdon, UK) was used for back-scatter electron (BSE) imaging and fast elemental analysis. Quantitative WDS elemental microanalyses of kaitianite and associated phases were carried out using a JEOL 8200 EPMA (JEOL Ltd., Tokyo, Japan) (15 kV and 10 nA, focused beam) interfaced with the probe for EPMA program. Standards for analysis were anorthite (Si*Ka*, Al*Ka*, Ca*Ka*), forsterite (Mg*Ka*), TiO_2 (Ti*Ka*), and zircon (Zr*La*). Quantitative elemental microanalyses were processed with the CITZAF correction procedure [18]. The focused electron beam was ~150 nm in diameter. Analytical results of kaitianite and associated phases are given in Table 1.

Table 1. EPMA analytical results (in wt%) for kaitianite, associated tistarite, Ti,Al,Zr-oxide, $MgTi^{3+}{}_2Al_4SiO_{12}$ phase, and sapphirine.

Oxide	Kaitianite	SD [b]	Tistarite	SD	Ti,Al,Zr-Oxide	SD	$MgTi^{3+}{}_2Al_4SiO_{12}$	SD	Sapphirine	SD
	$n = 6$ [a]		$n = 5$		$n = 7$		$n = 11$		$n = 5$	
SiO_2	0.02	0.01			2.72	0.21	11.95	0.19	11.55	0.08
Ti_2O_3	58.04	0.15	89.53	0.18	58.04	0.66	28.36	0.70	5.86	0.17
TiO_2	37.82	0.10	6.77	0.01						
Al_2O_3	2.87	0.03	0.88	0.04	21.27	0.37	45.73	0.81	63.21	0.19
MgO	0.85	0.01	3.37	0.03	1.86	0.13	9.67	0.08	18.78	0.07
CaO	0.02	0.01	0.02	0.01	0.02	0.01				
ZrO_2	0.10	0.24			13.53	0.74	3.88	0.37		
Total	99.72		100.57		97.44		99.64		99.40	
No. O atoms	5		3		3		12		20	
Si	0.00				0.06		0.90		1.36	
Ti^{3+}	1.78		1.74		1.10		1.79		0.58	
Ti^{4+}	1.05		0.12							
Al	0.12		0.02		0.57		4.08		8.75	
Mg	0.05		0.12		0.06		1.09		3.29	
Ca	0.00		0.00		0.00					
Zr	0.00				0.15		0.14			
Cation sum	3.00		2.00		1.95		20.01		33.98	

Note: [a] n = number of analyses. [b] SD = one standard deviation of the mean based on all of the analyses.

EBSD analyses at a submicrometer scale were performed using methods described in [19,20] for mineral identifications. An HKL EBSD system (Oxford Instruments, UK) on the ZEISS 1550VP Field-Emission SEM was operated at 20 kV and 6 nA in focused beam

mode with a 70° tilted stage and in a variable pressure mode (25 Pa). The EBSD system was calibrated using a single-crystal silicon standard. Structural information was obtained and cell constants were derived by matching the experimental EBSD patterns with structures of synthetic phases from the ICSD [21,22].

3. Results

Kaitianite occurs as exsolution lamellae in tistarite, in a melt inclusions together with a Ti,Al,Zr-oxide, a $MgTi^{3+}{}_2Al_4SiO_{12}$ phase, spinel, sapphirine, Ti-sulfide, alabandite, and Si-rich glass from the corundum xenocryst Grain 1125C2 (Figure 1). The grain was retrieved from a bulk sample. Other inclusions in this corundum grain contain krotite ($CaAl_2O_4$), grossite ($CaAl_4O_7$), osbornite (TiN), and Fe metal. Kaitianite is transparent, occurring as thin lamellae, ~0.1 to 2.5 µm thick, ~3 to 40 µm long.

The chemical composition of kaitianite using EPMA (Table 1) shows an empirical formula (based on 5 O pfu) of $(Ti^{3+}{}_{1.78}Al_{0.12}Ti^{4+}{}_{0.05}Mg_{0.05})_{\Sigma 2}(Ti^{4+}{}_{1.00})O_5$, where Ti^{3+} and Ti^{4+} are partitioned, assuming a stoichiometry with three cations and five oxygen anions pfu. The simplified formula is $(Ti^{3+},Al)_2Ti^{4+}O_5$, and the ideal formula is $Ti^{3+}{}_2Ti^{4+}O_5$. The EBSD patterns can be indexed only by the monoclinic $C2/c$ γ-Ti_3O_5-type structure and match the synthetic γ-Ti_3O_5 cell from [21] (Figure 2) with a mean angular deviation of ~0.38°, revealing the following cell parameters: a = 10.12 Å, b = 5.07 Å, c = 7.18 Å, β = 112°, V = 342 Å^3, and Z = 4.

Associated tistarite has an empirical formula of $(Ti^{3+}{}_{1.74}Ti^{4+}{}_{0.12}Mg_{0.12}Al_{0.02})_{\Sigma 2}O_3$. The Ti,Al,Zr-oxide is similar to the Allende Ti,Al,Zr-oxide [14]. The $MgTi^{3+}{}_2Al_4SiO_{12}$ phase has an empirical formula of $Mg_{1.09}Zr_{0.14}Ti^{3+}{}_{1.79}Al_{4.08}Si_{0.90}O_{12}$ and probably is a new mineral. Sapphirine has an empirical formula of $(Al_{4.11}Mg_{3.29}Ti^{3+}{}_{0.58})(Al_{4.64}Si_{1.36})O_{20}$.

The Ti-sulfide is a new mineral with an empirical formula of $(Ti_{1.10}Fe_{0.21}Cr_{0.17}Mn_{0.07}V_{0.01})_{\Sigma 1.56}S_{2.00}$ and the P-3m1 $TlCdS_2$-type. The general formula for this nonstoichiometric Ti-sulfide is $Ti_{1+x}S_2$.

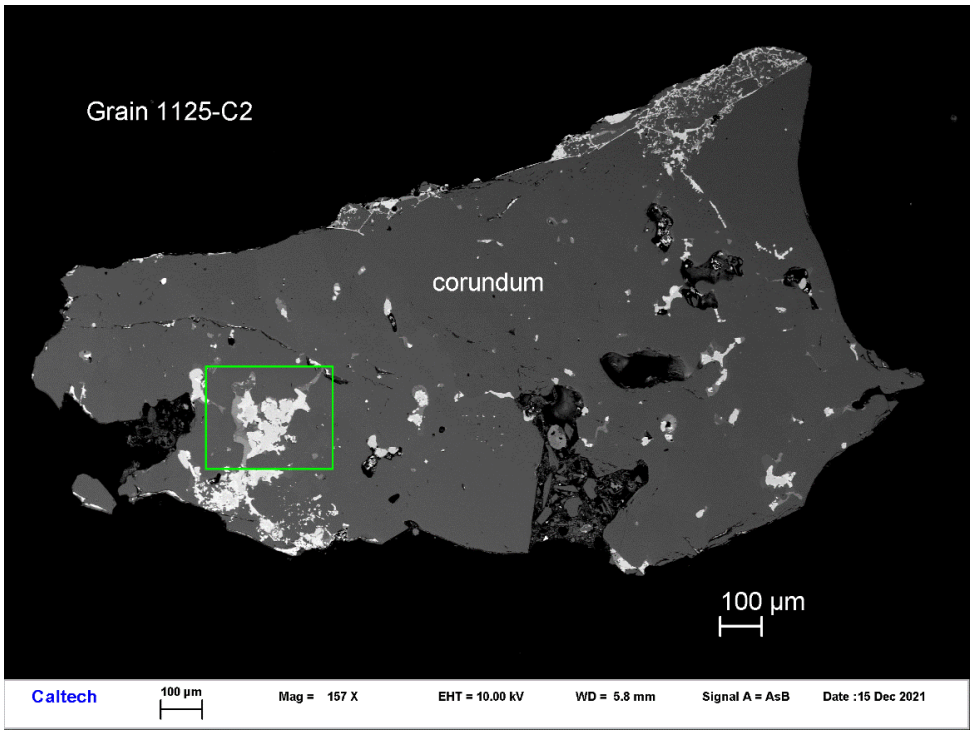

(**a**)

Figure 1. *Cont.*

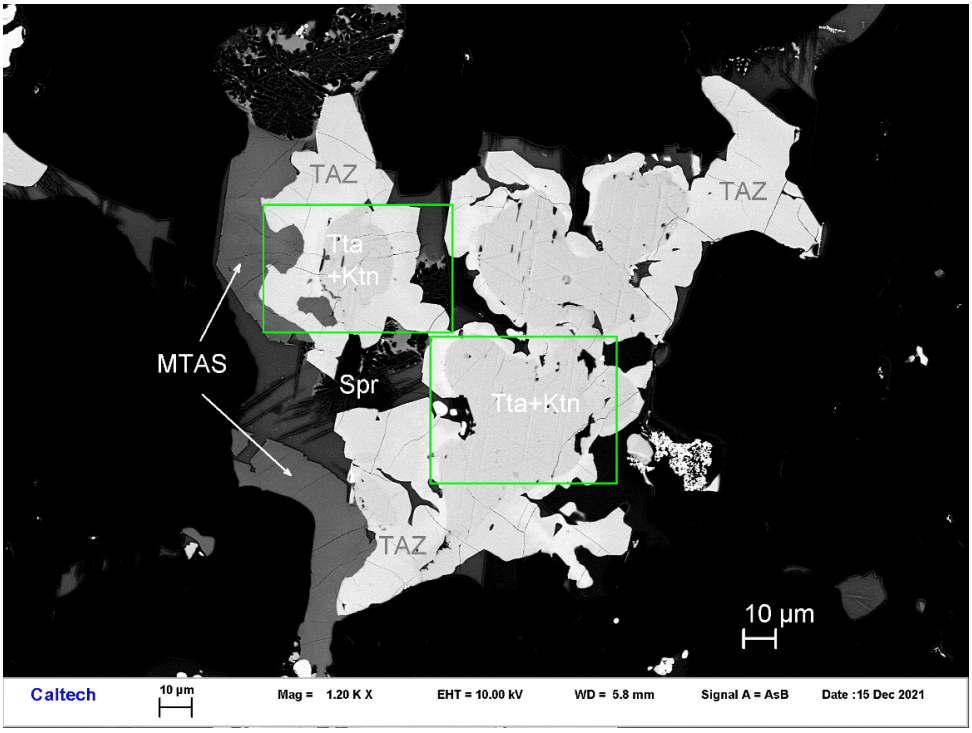

(**b**)

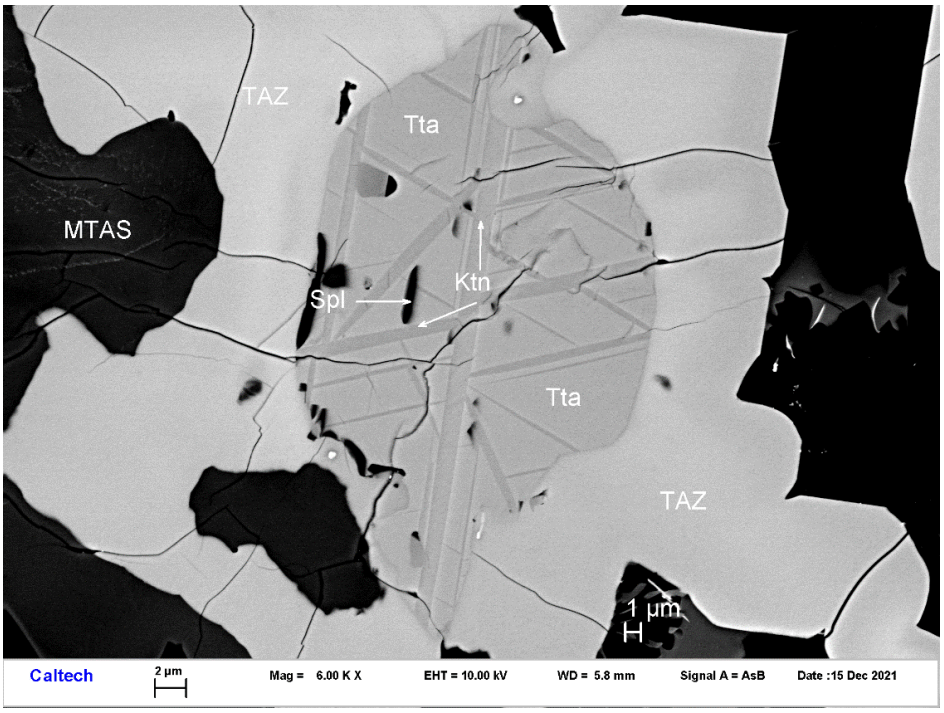

(**c**)

Figure 1. *Cont.*

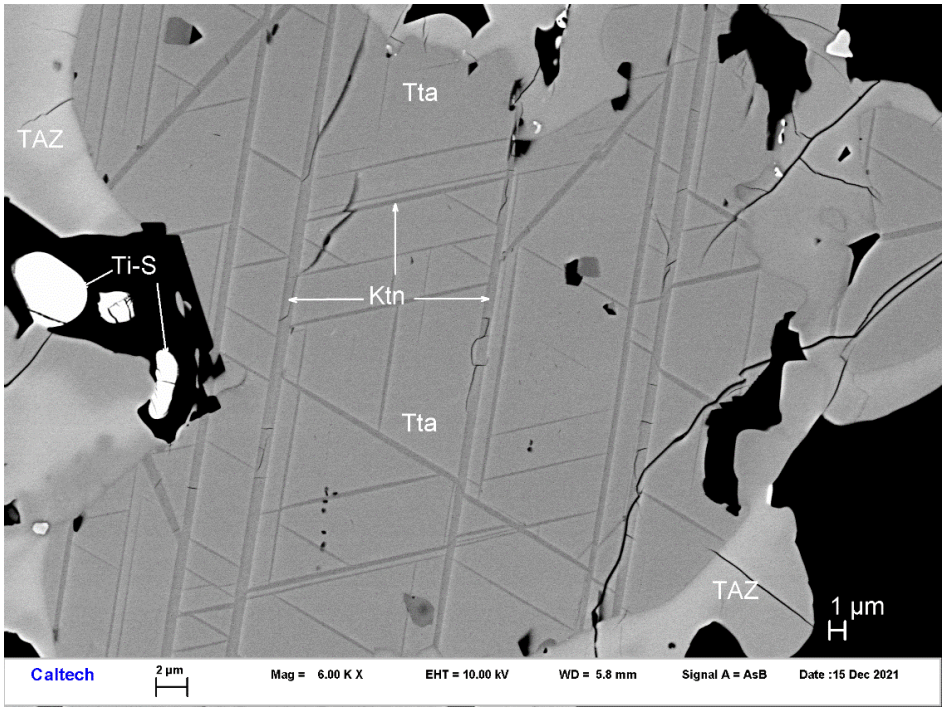

(**d**)

Figure 1. SEM BSE images showing kaitianite (Ktn) with tistarite (Tta), Ti,Al,Zr-oxide (TAZ), $MgTi^{3+}{}_2Al_4SiO_{12}$ phase (MTAS), spinel (Spl), sapphirine (Spr), and Ti-sulfide (Ti-S) in corundum Grain 1125C2. The rectangular area in (**a**) is enlarged in (**b**); the two rectangular areas in (**b**) are enlarged in (**c**,**d**).

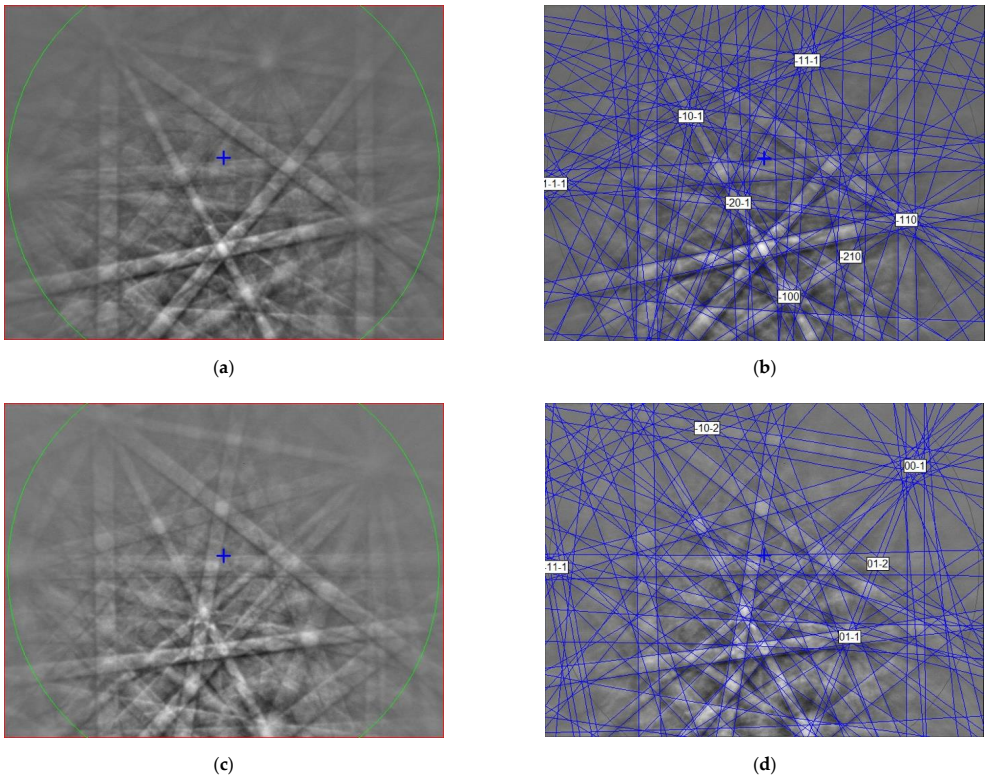

(**a**) (**b**)

(**c**) (**d**)

Figure 2. (**a**,**c**) EBSD patterns of the kaitianite crystals in Figure 1 at different orientations, and (**b**,**d**) the patterns indexed with the $C2/c$ γ-Ti_3O_5 structure. The blue cross shows pattern canter, the blue lines are calculated diffraction bands.

4. Discussion

Kaitianite ($Ti^{3+}{}_2Ti^{4+}O_5$) is γ-Ti_3O_5 [21]. The newly approved mineral sassite ($Ti^{3+}{}_2Ti^{4+}O_5$; IMA 2022-014) [10] is β-Ti_3O_5 [23,24], a member of the pseudobrookite group, joining pseudobrookite (Fe_2TiO_5), armalcolite ($(Mg,Fe^{2+})Ti_2O_5$), and griffinite (Al_2TiO_5; IMA 2021-110; [7]. Several polymorphs of Ti_3O_5 have been described so far: α–Ti_3O_5 having monoclinic symmetry, *C*2/*m*, with *a* = 9.752(1), *b* = 3.802(1), *c* = 9.442(1) Å and β = 91.55(1)° [25]; β-Ti_3O_5 having orthorhombic symmetry, *Cmcm*, *a* = 3.798(2), *b* = 9.846(3), *c* = 9.988(4) Å [24], which corresponds to sassite; γ-Ti_3O_5, having the monoclinic V_3O_5-type structure, and *a* = 10.115, *b* = 5.074, *c* = 7.182 Å, β = 112° and *C*2/*c* space group [21], which corresponds to kaitianite; δ–Ti_3O_5 that shows monoclinic structure and *P*2/*a* space group, with lattice parameters *a* = 9.9651(7), *b* = 5.0604(4), *c* = 7.2114(5) Å, and β = 109.3324(9)°, related to γ-Ti_3O_5 by decreasing temperature [22,26,27]; and λ–Ti_3O_5 which is monoclinic *C*2/*m* with *a* = 9.8357(11), *b* = 3.7935(2), *c* = 9.9863(7) Å, β = 90.976(6)° and related to α–Ti_3O_5 by a second-order phase transition [28]. The type kaitianite has been described as associated with tistarite and rutile, together with corundum, xifengite, mullite, osbornite, and a new Ti,Al,Zr-oxide mineral in the Allende CV3 carbonaceous chondrite [14]; most of these minerals are also present in the melt pockets in corundum aggregates from Mount Carmel.

Ti^{3+}-rich phases are common in melt inclusions in those corundum xenocrysts, including tistarite (Ti_2O_3), magnéliite ($Ti^{3+}{}_2Ti^{4+}{}_2O_7$), sassite ($Ti^{3+}{}_2Ti^{4+}O_5$), and kaitianite ($Ti^{3+}{}_2Ti^{4+}O_5$) (Figure 3). While low temperature α–Ti_3O_5 is highly ordered (three octahedral Ti sites, with <Ti–O> = 2.015 Å, 2.033 Å, and 2.033 Å), sassite and kaitianite show higher degrees of disorder (two crystallographically independent Ti sites, labeled Ti1 and Ti2, octahedrally surrounded by oxygen atoms, with <Ti1–O> = 2.0271 Å and <Ti2–O> = 2.0385 Å for sassite and <Ti1–O> = 2.0334 Å and <Ti2–O> = 2.0331 Å for kaitianite).

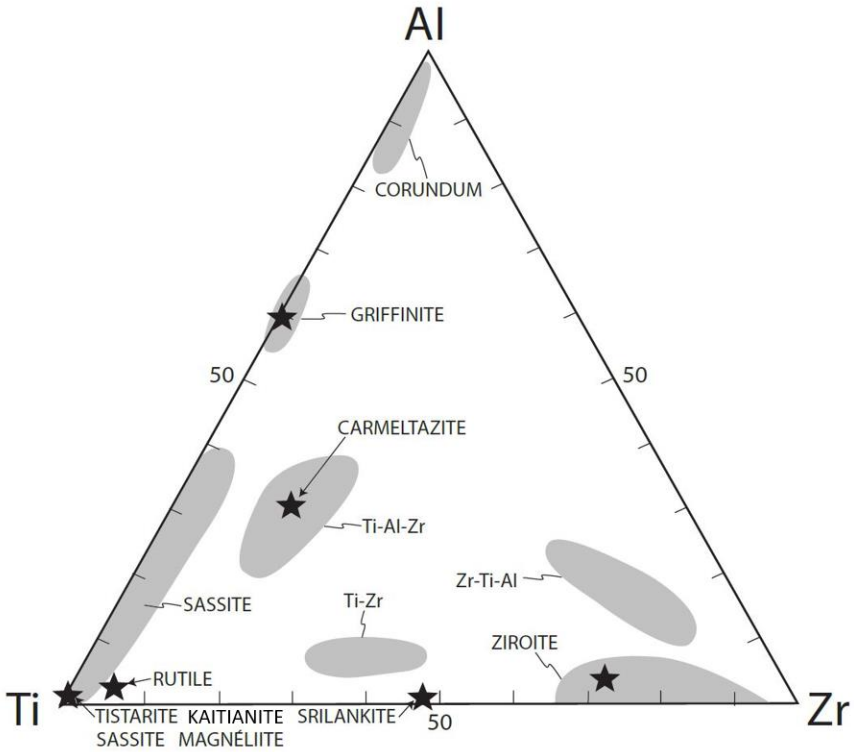

Figure 3. Ti-Al-Zr triplot showing phases with various compositions from melt inclusions in corundum xenocrysts from the Mount Carmel area.

Kaitianite and the associated minerals described here are high-temperature (>1300–ca. 1150 °C) phases, crystallized from melts trapped in intracrystalline and interstitial voids in aggregates of corundum crystals [6,15]. The whole suite is characterized by oxygen fugacity (fO_2) below the levels normally encountered in Earth's upper mantle or crust (IW

to IW-9; [29]). The most reduced parageneses, including hibonite + grossite + V^0, require a hydrogen-dominated environment, as confirmed by the occurrence of natural hydrides and spectroscopic evidence of hydrogen in vacancies in hibonite [17,29–31].

The super-reduced mineral assemblages evolved within a thick Triassic–Miocene gabbroic underplate and are ascribed to the progressive reduction and desilication of differentiated syenitic melts, through interaction with mantle-derived CH_4 + H_2 fluids [3,5,32]. The presence of these fluids is documented by the extremely low fO_2 recorded in associated parageneses, the abundance of carbon-bearing phases including SiC, TiC, Ti(N,C,O), and explosion breccias with amorphous-carbon matrices [2,5,17,29,32–34]. Voids bounded by crystal faces and sometimes populated by phenocryst phases can comprise >2% of some samples, implying the presence of a fluid phase, while some melt pockets contain bubbles, presumably gas-filled. Gasses released by ignition are typically ca. 95 at.% H_2 [5]. Desilication of the melts accompanied the separation of Fe–Ti–Si melts and Si^0 melts, driving saturation or supersaturation of Al_2O_3 in the silicate melts and leading to the crystallization of abundant corundum.

In the corundum aggregates, three broad paragenetic types have been recognized [3]:

Crn-A: hopper to skeletal crystals with strong zoning in Ti due to uptake of Ti^{3+} during rapid crystal growth [35]. Trapped melts are Ca–Mg–Al silicates with high contents of S and incompatible elements. Phase assemblages reflect $fO_2 \leq$ IW-6, with all Ti as Ti^{3+} (e.g., tistarite, carmeltazite) or Ti^{2+} (TiC, TiN, TiB_2, Ti-Fe alloys);

Crn-B: large homogeneous (unzoned) corundum crystals, typically with Ti contents > 1 wt%. Interstitial pockets contain small amounts of Ca–Al–Mg silicate glass, typically high in *REE*, Zr, Th, U, and other incompatible elements. Ti is present in phenocrysts as both Ti^{3+} and Ti^{4+}. Kaitianite is a member of this paragenesis and its occurrence as exsolution lamellae suggests an increase in fO_2 following the crystallization of tistarite, in which all Ti is Ti^{3+};

Crn-C: texturally similar to *Crn-B* but Ti contents in corundum typically are low (<0.5 wt% Ti). Rare Ca–Al–Na–K silicate glasses are rich in *LREE* and Ba. The presence of more Ti^{4+} phases (rutile, griffinite) suggests a higher mean fO_2 than in *Crn-A* and *Crn-B*. Hibonite occurs in all three parageneses; in *Crn-A* and *Crn-B*, it contains high levels of Ti^{3+}, while in *Crn-C* the Ti^{3+} contents are very low.

The identification of mixed-valence phases in paragenesis *Crn-B*, and possibly in *Crn-C*, adds new information relevant to the interpretation of the origins of the Mount Carmel corundum-aggregate xenoliths. Textural evidence indicates that *Crn-B* and *Crn-C* are cumulates from immiscible Fe-rich melts (subsequently depleted in Fe by the separation of Fe-Ti silicide melts; [5]) and Si–Al–Na–K melts, respectively. It seems probable that these melts, with similar but divergent histories, separated into volumes that were affected to different extents by the interaction with the reducing (CH_4 + H_2) fluids before being entrained in the host basalt. *Crn-A,* in contrast, appears to represent the very rapid crystallization of corundum in the presence of highly reducing (CH_4 + H_2) fluids and residual melts, possibly in melt-escape channels developed above magma chambers.

The details of the evolution of these remarkable parageneses are becoming steadily clearer through these nanomineralogical studies of the melt inclusions in the different corundum parageneses, and related types of xenoliths. Further surprises can be expected.

Author Contributions: Conceptualization, C.M., F.C., L.B. and W.L.G.; methodology, C.M.; formal analysis, C.M., F.C., L.B. and W.L.G.; investigation, C.M., F.C., L.B. and W.L.G.; resources, V.T.; data curation, C.M.; writing—original draft, C.M. and W.L.G.; writing—review and editing, C.M., F.C., L.B. and W.L.G. All authors have read and agreed to the published version of the manuscript.

Funding: The research was funded by MIUR-PRIN2017, project "TEOREM deciphering geological processes using Terrestrial and Extraterrestrial ORE Minerals", prot. 2017AK8C32 (PI: Luca Bindi).

Data Availability Statement: Data are available from C.M. and W.L.G.

Acknowledgments: SEM—EBSD and EPMA analyses were carried out at the Caltech GPS Division Analytical Facility, which is supported, in part, by NSF Grants EAR-0318518 and DMR-0080065. This is contribution 1773 from the ARC Centre of Excellence for Core to Crust Fluid Systems (http://www.ccfs.mq.edu.au) and 1541 in the GEMOC Key Centre (http://www.gemoc.mq.edu.au).

Conflicts of Interest: The authors declare no conflict of interest.

References

1. Xiong, Q.; Griffin, W.L.; Huang, J.-X.; Gain, S.E.M.; Toledo, V.; Pearson, N.J.; O'Reilly, S.Y. Super-reduced mineral assemblages in "ophiolitic" chromitites and peridotites: The view from Mt. Carmel. *Eur. J. Miner.* **2017**, *29*, 5. [CrossRef]
2. Griffin, W.L.; Huang, J.-X.; Thomassot, E.; Gain, S.E.M.; Toledo, V.; O'Reilly, S.Y. Super-reducing conditions in ancient and modern volcanic systems: Sources and behaviour of carbon-rich fluids in the lithospheric mantle. *Miner. Petrol.* **2018**, *112*, 101–114. [CrossRef]
3. Griffin, W.L.; Bindi, L.; Cámara, F.; Ma, C.; Gain, S.E.M.; Saunders, M.; Alard, O.; Huang, J.-X.; Shaw, J.; Meredith, C.; et al. Interactions of magmas and highly reduced fluids during intraplate volcanism, Mt Carmel, Israel: Implications for mantle redox states and global carbon cycles. *Gondwana Res.* 2023, *in review*.
4. Griffin, W.L.; Toledo, V.; O'Reilly, S.Y. Discussion of "Enigmatic super-reduced phases in corundum from natural rocks: Possible contamination from artificial abrasive materials or metallurgical slags" by Litasov et al. *Lithos* **2019**, *348*, 105122. [CrossRef]
5. Griffin, W.L.; Gain, S.E.M.; Saunders, M.; Huang, J.-X.; Alard, O.; Toledo, V.; O'Reilly, S.Y. Immiscible metallic melts in the upper mantle beneath Mount Carmel, Israel: Silicides, phosphides and carbides. *Am. Miner.* **2022**, *107*, 532–549. [CrossRef]
6. Griffin, W.L.; Toledo, V.; O'Reilly, S.Y. Discussion of paper by Galuskin and Galuskina, "Evidence of the anthropogenic origin of the "Carmel Sapphire" with enigmatic super-reduced minerals". *Miner. Mag.* **2023**, *87*, 631–634. [CrossRef]
7. Ma, C.; Bindi, L.; Cámara, F.; Toledo, V. Griffinite, IMA 2021-110, in: CNMNC Newsletter 66. *Eur. J. Miner.* **2022**, *34*, 253–257.
8. Ma, C.; Griffin, W.L.; Bindi, L.; Cámara, F.; Toledo, V. Magnéliite, IMA 2021-111, in CNMNC Newsletter 66. *Miner. Mag.* **2022**, *86*, 362.
9. Ma, C.; Griffin, W.L.; Bindi, L.; Cámara, F.; Toledo, V. Ziroite, IMA 2022-013, in CNMNC Newsletter 68. *Miner. Mag.* **2022**, *86*, 854–855.
10. Ma, C.; Griffin, W.L.; Bindi, L.; Cámara, F.; Toledo, V. Sassite, IMA 2022-014, in CNMNC Newsletter 68. *Miner. Mag.* **2022**, *86*, 855.
11. Ma, C.; Griffin, W.L.; Bindi, L.; Cámara, F.; Toledo, V. Mizraite-(Ce), IMA 2022-027, in CNMNC Newsletter 68. *Miner. Mag.* **2022**, *86*, 857.
12. Ma, C.; Griffin, W.L.; Bindi, L.; Cámara, F. Toledoite, IMA 2022-036, in CNMNC Newsletter 66. *Miner. Mag.* **2022**, *86*, 858.
13. Ma, C.; Griffin, W.L.; Bindi, L.; Cámara, F.; Toledo, V. Yeite, IMA 2022-079, in CNMNC Newsletter 70. *Miner. Mag.* **2023**, *87*, 165.
14. Ma, C.; Beckett, J.R. Kaitianite, $Ti^{3+}{}_2Ti^{4+}O_5$, a new titanium oxide mineral from Allende. *Meteorit. Planet. Sci.* **2021**, *56*, 96–107. [CrossRef]
15. Griffin, W.L.; Gain, S.E.M.; Bindi, L.; Toledo, V.; Cámara, F.; Saunders, M.; O'Reilly, S.Y. Carmeltazite, $ZrAl_2Ti_4O_{11}$, a new mineral trapped in corundum from volcanic rocks of Mt Carmel, northern Israel. *Minerals* **2018**, *8*, 601. [CrossRef]
16. Griffin, W.L.; Gain, S.E.M.; Adams, D.T.; Huang, J.-X.; Saunders, M.; Toledo, V.; Pearson, N.J.; O'Reilly, S.Y. First terrestrial occurrence of tistarite (Ti_2O_3): Ultra-low oxygen fugacity in the upper mantle beneath Mt Carmel, Israel. *Geology* **2016**, *44*, 815–818. [CrossRef]
17. Griffin, W.L.; Gain, S.E.M.; Huang, J.-X.; Saunders, M.; Shaw, J.; Toledo, V.; O'Reilly, S.Y. A terrestrial magmatic hibonite-grossite-vanadium assemblage: Desilication and extreme reduction in a volcanic plumbing system, Mount Carmel, Israel. *Am. Miner.* **2019**, *104*, 207–217. [CrossRef]
18. Armstrong, J.T. CITZAF: A package of correction programs for the quantitative electron microbeam X-ray analysis of thick polished materials, thin films, and particles. *Microbeam Anal.* **1995**, *4*, 177–200.
19. Ma, C.; Rossman, G.R. Barioperovskite $BaTiO_3$, a new mineral from the Benitoite Mine, California. *Am. Miner.* **2008**, *93*, 154–157. [CrossRef]
20. Ma, C.; Rossman, G.R. Tistarite, Ti_2O_3, a new refractory mineral from the Allende meteorite. *Am. Miner.* **2009**, *94*, 841–844. [CrossRef]
21. Hong, S.-H.; Åsbrink, S. The structure of γ-Ti_3O_5 at 297 K. *Acta Crystallogr. B* **1982**, *38*, 2570–2576. [CrossRef]
22. Tanaka, K.; Nasu, T.; Miyamoto, Y.; Ozaki, N.; Tanaka, S.; Nagata, T.; Hakoe, F.; Yoshikiyo, M.; Nakagawa, K.; Umeta, Y.; et al. Structural phase transition between γ-Ti_3O_5 and δ-Ti_3O_5 by breaking of a one-dimensionally conducting pathway. *Cryst. Growth Des.* **2015**, *15*, 653–657. [CrossRef]
23. Rusakov, A.A.; Zhdanov, G.S. The crystal structure and the chemical formula of titanic oxide Ti_3O_5 (Anosovite). *Doklady Akademii Nauk SSSR* **1951**, *77*, 411–414.
24. Onoda, M. Phase transitions of Ti_3O_5. *J. Solid State Chem.* **1998**, *136*, 67–73. [CrossRef]
25. Åsbrink, S.; Magnéli, A. Crystal structure studies on trititanium pentoxide, Ti_3O_5. *Acta Crystallogr.* **1959**, *12*, 575–581. [CrossRef]
26. Åsbrink, G.; Åsbrink, S.; Magnéli, A.; Okinaka, H.; Kosuge, K.; Kachi, S. A Ti_3O_5 modification of V_3O_5-type structure. *Acta Chem. Scand.* **1971**, *25*, 3889–3890. [CrossRef]

27. Åsbrink, S.; Pietraszko, A. Bond diffractometer measurements on Ti_3O_5 in the temperature region 90 to 720 K. *Phys. Status Solidi* **1991**, *128*, K77–K81. [CrossRef]
28. Ohkoshi, S.; Tsunobuchi, Y.; Matsuda, T.; Hashimoto, K.; Namai, A.; Hakoe, F.; Tokoro, H. Synthesis of a metal oxide with a room-temperature photoreversible phase transition. *Nat. Chem.* **2010**, *2*, 539–545. [CrossRef] [PubMed]
29. Griffin, W.L.; Gain, S.E.M.; Cámara, F.; Bindi, L.; Shaw, J.; Alard, O.; Saunders, M.; Huang, J.-X.; Toledo, V.; O'Reilly, S.Y. Extreme reduction: Mantle-derived oxide xenoliths from a hydrogen-rich environment. *Lithos* **2020**, *358*, 105404. [CrossRef]
30. Bindi, L.; Cámara, F.; Griffin, W.L.; Huang, J.-X.; Gain, S.E.M.; Toledo, V.; O'Reilly, S.Y. Discovery of the first natural hydride. *Am. Miner.* **2019**, *104*, 611–614. [CrossRef]
31. Bindi, L.; Cámara, F.; Gain, S.E.M.; Griffin, W.L.; Huang, J.-X.; Saunders, M.; Toledo, V. Kishonite, VH_2, and oreillyite, Cr_2N, two new minerals from the corundum xenocrysts of Mt Carmel, Northern Israel. *Minerals* **2020**, *10*, 1118. [CrossRef]
32. Griffin, W.L.; Gain, S.E.M.; Saunders, M.; Cámara, F.; Bindi, L.; Spartà, D.; Toledo, V.; O'Reilly, S.Y. Cr_2O_3 in corundum: Ultra-high contents under reducing conditions. *Am. Miner.* **2021**, *106*, 1420–1437. [CrossRef]
33. Griffin, W.L.; Gain, S.E.M.; Saunders, M.; Alard, O.; Shaw, J.; Toledo, V.; O'Reilly, S.Y. Nitrogen under super-reducing conditions: Ti oxynitride melts in xenolithic corundum aggregates from Mt Carmel (N. Israel). *Minerals* **2021**, *11*, 780. [CrossRef]
34. Huang, J.-X.; Xiong, Q.; Gain, S.E.M.; Griffin, W.L.; Murphy, T.D.; Siryaev, A.A.; Li, L.; Toledo, V.; Tomshin, M.D.; O'Reilly, S.Y. Immiscible metallic melts in the deep Earth: Clues from moissanite (SiC) in volcanic rocks. *Sci. Bull.* **2020**, *65*, 1479–1488. [CrossRef]
35. Oliviera, B.B.; Griffin, W.L.; Gain, S.E.M.; Saunders, M.; Shaw, J.; Toledo, V.; Afonso, J.C.; O'Reilly, S.Y. Ti^{3+} in corundum traces crystal growth in a highly reduced magma. *Sci. Rep.* **2021**, *11*, 2439. [CrossRef]